

3D MR Fingerprinting for Dynamic Contrast-Enhanced Imaging of Whole Mouse Brain

Yuran Zhu¹, Guanhua Wang², Yuning Gu¹, Walter Zhao¹, Jiahao Lu¹, Junqing Zhu³, Christina J. MacAskill¹, Andrew Dupuis¹, Mark A. Griswold^{1,3}, Dan Ma^{1,3}, Chris A. Flask^{1,3,4}, Xin Yu^{1,3,5}

¹Department of Biomedical Engineering, Case Western Reserve University, Cleveland, Ohio, USA

²Department of Biomedical Engineering, University of Michigan, Ann Arbor, Michigan, USA

³Department of Radiology, Case Western Reserve University, Cleveland, Ohio, USA

⁴Department of Pediatrics, Case Western Reserve University, Cleveland, Ohio, USA

⁵Department of Physiology and Biophysics, Case Western Reserve University, Cleveland, Ohio, USA

Submitted to Magnetic Resonance in Medicine

Word count: 3,925

Figure + table count: 8

Conflict of interest: None

Address correspondence to:

Xin Yu, Sc.D.,
Wickenden 430
10900 Euclid Avenue
Cleveland, OH 44106, USA
Tel: 216-368-3918
Email: xin.yu@case.edu

Abstract

Purpose: Quantitative MRI enables direct quantification of contrast agent concentrations in contrast-enhanced scans. However, the lengthy scan times required by conventional methods are inadequate for tracking contrast agent transport dynamically in mouse brain. We developed a 3D MR fingerprinting (MRF) method for simultaneous T_1 and T_2 mapping across the whole mouse brain with 4.3-min temporal resolution.

Method: We designed a 3D MRF sequence with variable acquisition segment lengths and magnetization preparations on a 9.4T preclinical MRI scanner. Model-based reconstruction approaches were employed to improve the accuracy and speed of MRF acquisition. The method's accuracy for T_1 and T_2 measurements was validated in vitro, while its repeatability of T_1 and T_2 measurements was evaluated in vivo (n=3). The utility of the 3D MRF sequence for dynamic tracking of intracisternally infused Gd-DTPA in the whole mouse brain was demonstrated (n=5).

Results: Phantom studies confirmed accurate T_1 and T_2 measurements by 3D MRF with an undersampling factor up to 48. Dynamic contrast-enhanced (DCE) MRF scans achieved a spatial resolution of $192 \times 192 \times 500 \mu\text{m}^3$ and a temporal resolution of 4.3 min, allowing for the analysis and comparison of dynamic changes in concentration and transport kinetics of intracisternally infused Gd-DTPA across brain regions. The sequence also enabled highly repeatable, high-resolution T_1 and T_2 mapping of the whole mouse brain ($192 \times 192 \times 250 \mu\text{m}^3$) in 30 min.

Conclusion: We present the first dynamic and multi-parametric approach for quantitatively tracking contrast agent transport in the mouse brain using 3D MRF.

Keywords: MR fingerprinting; 3D; dynamic contrast-enhanced; T_1 ; T_2 ; CSF

1. Introduction

Magnetic resonance imaging (MRI) of mouse brain provides invaluable insights into the pathophysiology of neurological disorders and contributes to the advancement of novel therapeutic interventions.¹ Among the tissue parameters measurable by MRI, the longitudinal (T_1) and transverse (T_2) relaxation times are of particular interest due to their sensitivity to pathological changes within the tissue, allowing them to serve as critical biomarkers.² Measuring T_1 and T_2 by quantitative MR (qMR) methods provides standardized and reproducible evaluations of disease progression and response to therapy.³ Furthermore, in cases of dynamic contrast-enhanced (DCE) imaging, quantifying T_1 and T_2 changes enables tracking of concentration changes of the contrast agents, thereby supporting pharmacokinetic modeling of tracer dynamics within the system.^{4,5} However, the conventional approaches cannot dynamically measure contrast agent transport across the whole mouse brain with sufficient spatial and temporal resolution.^{6–8}

Magnetic resonance fingerprinting (MRF) has emerged as an accurate and efficient method for simultaneously mapping multiple tissue parameters in a single scan with unprecedented speed.⁹ Although now widely implemented and evaluated in human studies,¹⁰ few studies have been conducted to exploit MRF's potential as an investigative tool for basic science studies in mouse.^{11–14} The development of MRF for imaging mouse brain has been greatly challenged by the significantly lower signal-to-noise ratio (SNR) due to the submillimeter voxel size needed to delineate mouse brain.¹⁵ Existing two-dimensional (2D) preclinical MRF sequences have proven to be fast and effective for studying healthy and diseased mouse brains and other tissues.^{11,12} These 2D MRF methods have also facilitated the dynamic quantification of contrast agent transport in tumor-bearing mouse models.^{12,16} However, the three-dimensional (3D) implementations have suffered from unacceptably prolonged scan time. A previous attempt to map whole-brain T_1 and T_2 in rat required 1.5 hrs to achieve a 0.5-mm isotropic resolution with a Cartesian trajectory, rendering the assessment of contrast agent dynamics unfeasible.¹⁴ Similarly, we recently implemented a stack-of-spirals trajectory to achieve a spatial resolution of $0.35 \times 0.35 \times 1 \text{ mm}^3$ for simultaneous T_1 and T_2 mapping across the entire macaque brain at 9.4 T in 1.8 hrs.¹⁷ While the study showed promise, further improvement in temporal and spatial resolutions is necessary to allow for efficient multiparametric mapping of the entire mouse brain.

In this study, we developed a 3D MRF sequence for simultaneous multiparametric mapping of the whole mouse brain with unparalleled speed and spatial resolution. The sequence acquired different numbers of time frames following the inversion and T_2 preparations to more

efficiently capture image contrast generated by the preparation modules. Iterative image reconstruction by subspace-based low-rank modeling was implemented on graphic processing units (GPUs) to improve the accuracy and efficiency of multiparametric mapping. The MRF sequence's accuracy in estimating T_1 and T_2 was validated through in vitro phantom studies. This method enabled T_1 and T_2 mapping in whole mouse brain at a spatial resolution of $192 \times 192 \times 250 \mu\text{m}^3$ in 30 min. We also demonstrated its application in dynamically and quantitatively tracking the transport of a gadolinium-based contrast agent (GBCA) in cerebrospinal fluid (CSF) after its intracisternal infusion, where 32 MRF scans of 4.3-min temporal resolution and $192 \times 192 \times 500 \mu\text{m}^3$ spatial resolution were collected.

2. Methods

2.1 MRF pulse sequence and data acquisition

The MRF sequence was partitioned into 8 segments with different magnetization preparations to encode T_1 , T_2 , and M_0 sensitivity (Figure 1). Specifically, an adiabatic inversion pulse was applied before segments 1 and 5, with an inversion time of 21 ms to enhance T_1 sensitivity. T_2 -preparation modules were applied before segments 3, 4, 7, and 8, with varying mixing times of 25 ms, 50 ms, 75 ms, and 100 ms, respectively.^{17,18} The acquisition of varying numbers of time frames in each segment was tailored to more effectively capture the T_1 , T_2 , and M_0 contrasts produced by the preparation module preceding the segment. A total of 768 frames were acquired using fast imaging with steady-state precession (FISP) scheme with a constant repetition time (TR) of 10 ms, a constant echo time (TE) of 2 ms, and a dephasing gradient of 4π .¹⁹ All excitations used a 1.5-ms sinc pulse with 7 lobes. A varying flip angle (FA) pattern with low nominal angles ($<15^\circ$) was used to reduce the influences of B_1 inhomogeneity.²⁰ A 300-ms delay was applied between two consecutive acquisition segments and a 3-s delay was applied after one fingerprint acquisition to allow partial magnetization recovery. The acquisition time of a single fingerprint was ~ 13 s.

A stack-of-spirals trajectory was used to acquire the 3D MRF data.²¹ Two uniform density spiral (UDS) trajectories with a readout bandwidth of 200 kHz were designed for in vitro and in vivo studies, respectively. For in vitro studies on phantoms, a field of view (FOV) of $50 \times 50 \text{ mm}^2$ was sampled with a matrix size of 256×256 , leading to an in-plane resolution of $195 \times 195 \mu\text{m}^2$. For in vivo studies, FOV and matrix size were $30 \times 30 \text{ mm}^2$ and 156×156 , respectively, yielding

an in-plane resolution of $192 \times 192 \mu\text{m}^2$. The readout time of a single spiral interleaf was 4.1 and 2.9 ms for in vitro and in vivo scans, respectively.

The spiral trajectories fully sampled the k-space with 48 spiral arms, and the rotation angle between two adjacent spiral arms was 7.5° ($360^\circ/48$). Acceleration of data acquisition was achieved by undersampling in both the in-plane (k_{xy}) and through-plane (k_z) directions as described previously.^{17,21} For scans with an in-plane undersampling factor of R_{xy} , $48/R_{xy}$ spiral arms with a rotation angle of $R_{xy} \times 7.5^\circ$ were sampled in each frame. Within each fingerprint acquisition, the spiral arms were rotated by 7.5° from one frame to the next. For through-plane sampling with an undersampling factor of R_z , the k_z lines were divided into partitions with R_z lines in each partition. Undersampling was achieved by acquiring one fingerprint from each partition and cycling the acquisition of the R_z lines within the same partition repeatedly across all the time frames.

2.2 Dictionary simulation

A dictionary of simulated fingerprints was generated by solving the Bloch equation using the acquisition parameters of the MRF sequence. Specifically, the signal evolution was simulated as the vector sum of 81 isochromats experiencing 4π dephasing at the end of each TR. Variable step sizes were used to generate the T_1 and T_2 entries for the dictionary, where the T_1 and T_2 values were more densely distributed in the range of brain parenchyma in pre- and post-contrast conditions.^{12,17} In particular, a 20-ms step size was used for T_1 and a 0.5-ms step size was used for T_2 at the more dense regions. T_1 step size incremented to 200 ms beyond 2000 ms. The T_2 step size was adjusted to 2 ms for values between 40 and 60 ms, increased to 10 ms for values between 60 and 200 ms, and set to 20 ms for values over 200 ms. A total of 126 T_1 values from 100 ms to 8000 ms and 111 T_2 values from 2 ms to 400 ms were used, leading to 13,986 dictionary entries in total.

2.3 Image reconstruction

Iterative image reconstruction was employed with low-rank (LR) subspace modeling to mitigate aliasing artifacts from undersampling.²² The MRF data, as a time series of images, can be represented as a Casorati matrix ($C^{N \times M}$), with spatial and temporal dimensions represented by its rows (N) and columns (M), respectively. A low-rank constraint can be enforced on C to exploit the strong spatial-temporal correlation within the acquired MRF data. Specifically, a Casorati matrix of rank L ($L \ll N, M$) can be factorized into two matrices $U^{N \times L}$ and $V^{L \times M}$, i.e., $C =$

UV , with the rows of U and columns of V span the spatial and temporal subspaces of C , respectively.²³ The image reconstruction for MRF can thus be estimated iteratively by minimizing the following cost function

$$\hat{U} = \arg \min_U \left\| AU\hat{V} - y \right\|_2^2 + \lambda \phi(U)$$

where A represents the system encoding matrix that spans all receiver channels, MRF time frames, and sampled k-space dimensions within each time frame. $\phi(U)$ denotes an L1 regularizer, i.e., $\phi(U) = \|U\|_1$, with the weight λ chosen from a grid search. The temporal pre-estimation, \hat{V} , was extracted from the singular value decomposition (SVD) of the simulated MRF dictionary. The rank of the model (L) was heuristically determined, and a rank of 12 reflected the low-rank constraint that the singular value of the dictionary had decayed by >90%.

All image reconstruction and dictionary matching were performed using PyTorch on an Nvidia Tesla V100 GPU. Coil sensitivity maps were calculated from the time-series-compressed MRF data by ESPIRiT.^{24,25} The conjugate gradient (CG) and Fast Iterative Shrinkage-Thresholding Algorithm (FISTA) were employed to iteratively solve the smooth ($\lambda = 0$) and non-smooth ($\lambda > 0$) cost functions, respectively.^{26,27} The convergence was empirically determined based on the residual norm ($\|AU\hat{V} - y\| / \|y\|$).²⁸ The LR-based image reconstruction method was compared with the conventional reconstruction through the inverse non-uniform fast Fourier transform (iNUFFT).²⁹ Both conventional and LR-based image reconstructions were executed using an open-source toolkit, MIRTorch.^{30,31} Leveraging Toeplitz embedding and data parallelism, the reconstruction time of the LR algorithm was significantly accelerated for each 3D MRF scan on our current hardware.³²

2.4 In vitro validation in phantom

All MRI studies were performed on a 9.4T Bruker BioSpin system (Bruker Biospin, Billerica, MA). A 6-compartment phantom containing different concentrations of manganese chloride ($MnCl_2$, 50 to 300 μM) was used to mimic the T_1 and T_2 values in brain parenchyma at 9.4 T.^{12,17} A 40-mm transmit/receive volume coil was used for data acquisition. MRF data were acquired from 20 slices with an in-plane resolution of $195 \times 195 \mu m^2$ and a thickness of 0.5 mm. The acquisition of a fully sampled dataset was about 3 hr 28 min. Retrospective undersampling was performed on the fully sampled MRF data to evaluate different undersampling schemes, and the accuracies of T_1 and T_2 estimation were compared against the results of fully sampled data. T_1

and T_2 maps of the center slice were also acquired using conventional methods, with a lower resolution of $468 \times 468 \mu\text{m}^2$. Specifically, T_1 was measured using the inversion-recovery spin-echo (IR-SE) method with 15 inversion times (TIs) ranging from 10 ms to 6 s. TR and TE were 10 s and 4.6 ms, respectively. T_2 was measured using the spin-echo method with 15 TEs ranging from 4 ms to 800 ms and a constant TR of 10 s.

2.5 In vivo experiments

The animal protocol was approved by the Institutional Animal Care and Use Committee (IACUC) of Case Western Reserve University. All experiments were performed on male C57BL/6 mice (Jackson Laboratories, Bar Harbor, ME, USA). The animals were housed in a temperature- and humidity-controlled environment with ad libitum access to food and water and a 12-h light-dark cycle. Anesthesia was maintained with 1-1.5% isoflurane in 100% O_2 during all surgical procedures and MRI scans. All MRI acquisitions used an 86-mm volume coil for transmitting and a 4-channel array coil for receiving. Respiration rate and body temperature were monitored during all MRI experiments. The respiratory rate was maintained within 90 to 110 breaths per minute (bpm) by adjusting the anesthesia level. The body temperature was maintained at $\sim 37^\circ\text{C}$ by blowing warm air into the scanner through a feedback control system (SA Instruments, Stony Brook, NY, US).

T_1 and T_2 maps of the whole mouse brain were acquired by 3D MRF with 24-fold undersampling ($n=3$). Imaging parameters were: FOV, $30 \times 30 \times 17.5 \text{ mm}^3$; matrix size, $156 \times 156 \times 70$; slice thickness, 0.25 mm; in-plane resolution, $192 \times 192 \mu\text{m}^2$. Total scan time was ~ 30 min. T_2 -weighted (T_2w) images with matching FOV and spatial resolution were also acquired using a multislice RARE sequence with a TR of 4000 ms and an effective TE of 25.8 ms. The MRF measurements of T_1 and T_2 were repeated on different days to evaluate the reproducibility of the proposed method. All mice were 14 weeks old, and the average body weight was 31.1 g at the time of MRI experiments.

Dynamic MRF scans were performed on mice with intracisternal infusion of Gd-DTPA ($n = 5$). Intracisternal cannulation of a polyethylene micro-tubing (0.13 mm ID \times 0.25 mm OD, Scientific Commodities, Lake Havasu City, AZ, USA) was performed before MRI scans as previously described.³³ All mice were 10-12 weeks old at the time of the experiment and had an average body weight of 27.1 g. An undersampling factor of 48 was used for dynamic mapping with a temporal resolution of 4 min 20 s. A total of 20 sagittal slices of 0.5-mm thickness that

covered the whole brain were acquired, with the same in-plane resolution as used in the anatomical mapping ($192 \times 192 \mu\text{m}^2$). One MRF dataset was acquired at baseline before Gd-DTPA infusion, followed by 31 MRF scans, for a total scan time of 135 min. A total of 10 μL Gd-DTPA of 12.5 mM concentration was infused at a rate of 0.33 $\mu\text{L}/\text{min}$ for 30 min after the baseline MRF acquisition.

2.6 Data analysis

All image and data analyses were performed using either in-house developed or open-source software in MATLAB (MathWorks, Natick, MA, USA) or Python (Python Software Foundation, v.3.0). All MRF maps were reconstructed using the LR method. For repeatability study, MRF-derived parameter maps from two different days were co-registered to an MRI mouse brain atlas using the Advanced Normalization Tools (ANTs),^{34–37} and mean T_1 and T_2 values in 13 regions of interest (ROIs) were calculated. For dynamic study, motion correction was performed by registering the dynamic maps to the baseline via affine transformation. 11 ROIs at major anatomical landmarks were manually selected. Dynamic changes in relaxation rates from baseline (ΔR_1 and ΔR_2) were calculated from the dynamic T_1 and T_2 maps. Subsequently, mean dynamic curves were obtained without normalization.

3. Results

3.1 T_1 and T_2 validation in phantom

The accuracy of T_1 and T_2 measurements from MRF scans at different undersampling factors was first validated in the multi-compartment phantom with iNUFFT-based image reconstruction. The compartment-wise mean T_1 and T_2 values measured at $R = 48$ were in excellent agreement with the IR-SE and SE measurements, respectively (Figure 2c,f). The R_1 and R_2 values derived from 48-fold undersampled MRF also demonstrated a linear relationship to Mn^{2+} concentrations and the calculated relaxivities were in strong agreement with those derived from IR-SE or SE methods, respectively (Figure S1).

LR reconstruction mitigated the aliasing artifacts from undersampling (Figure S2), leading to reduced compartment-wise standard deviations of T_1 and T_2 estimations at $R = 48$ (Figure 2a,d). The normalized root-mean-squared error (NRMSE) of MRF-derived T_1 and T_2 maps was evaluated at different undersampling factors for both iNUFFT- and LR-based image reconstructions (Figure 2b,e). Both T_1 and T_2 NRMSEs were under 10% at $R = 48$ when reconstructed with LR as compared to fully sampled MRF. The rate of residual decay was

evaluated on the 48-fold undersampled phantom data across 50 iterations of CG (Figure S3). Significant convergence was achieved by 20 iterations, with the subsequent iterations showing minimal residual decay. The entire LR-based reconstruction pipeline runs in under 20 min, thus enabling the efficient reconstruction of dynamic MRF scans. Based on these results, 48-fold undersampling using LR reconstruction was determined to be both accurate and efficient for DCE-MRF, leading to a temporal resolution of 4 min 20 s for dynamic, simultaneous T_1 and T_2 mapping at a spatial resolution of $192 \times 192 \times 500 \mu\text{m}^3$.

3.2 Mapping of T_1 and T_2 in the whole brain

T_1 and T_2 maps acquired with a slice thickness of 0.25 mm and 24-fold undersampling rate are shown in Figures 3-4, along with T_2w images for comparison of anatomic structures. The excellent delineation of major anatomic structures can be appreciated in all three views. In particular, MRF was able to differentiate gray and white matter across the whole brain, and delineate small structures such as the horns of the anterior commissure and corpus callosum (Figure 3). Fine anatomical details such as the corpus callosum are also discernible from the coronal and sagittal views (Figure 4). Major cerebral arteries were also notable on these T_1 and T_2 maps (Figure 4b), although there was an underestimation in measured T_1 and T_2 values of the blood due to flow effects.³⁸

Figure 5 shows MRF-measured T_1 and T_2 values from 13 regions. Among all parenchymal regions analyzed, the internal capsule exhibited the lowest average T_1 (1453 ± 109 ms) and T_2 (22.1 ± 1.9 ms) values, while olfactory bulbs showed the highest ($T_1 = 1914 \pm 150$ ms; $T_2 = 33.2 \pm 3.3$ ms). Furthermore, the T_1 and T_2 values of CSF in the ventricular spaces were 3091 ± 168 ms and 143.8 ± 17.2 ms, respectively.

The repeatability of MRF measurements was evaluated in vivo from two scans performed on two different days ($n = 3$). Matching anatomical details can be appreciated in all three orthogonal views from co-registered maps (Figure 6a-b). The voxel-wise correlation coefficients (r) between the T_1 and T_2 maps from the two scans exceeded 0.96, suggesting high repeatability (Figure 6c-d).

3.4 Quantitative and dynamic mapping of Gd-DTPA transport in CSF

Figures 7 and 8 show dynamic changes in T_1 and T_2 before, during, and after Gd-DTPA infusion. The 3D MRF scans, with a temporal resolution of 4 min 20 s, effectively captured the dynamic changes induced by the intracisternal Gd-DTPA infusion in the whole brain, allowing quantitative tracking of contrast agent transport over time. Gd-DTPA infusion induced a substantial decrease in T_1 (>1 s) in ROIs proximal to the infusion site, including cisterna magna, cerebellum, and the lower brain stem (Figure 7b). The T_2 changes in these regions were relatively small. While the cerebellum and lower brain stem experienced fast Gd-DTPA transport kinetics and high peak Gd-DTPA concentrations, the ΔR_1 increase in colliculi was significantly delayed, indicating an impediment in the transport of Gd-DTPA to this midbrain region from cisterna magna. In the meantime, Gd-DTPA transport along the ventral brain surface is prominent in both the T_1 maps and the time courses of ΔR_1 changes in these regions (Figure 7c). ROIs along the ventral brain surface showed a progressive increase in Gd-DTPA concentration accompanied by a reduction in peak concentration from posterior to anterior directions. Delayed transport kinetics and a 10-fold smaller Gd-DTPA magnitude can also be appreciated in the ROIs along the ventral brain surface as compared to those adjacent to the infusion site. The change in Gd-DTPA concentration reflected by both ΔR_1 and ΔR_2 changes were negligible in dorsal and deep brain regions except for hippocampus, suggesting that they are downstream of the Gd-DTPA transport (Figures 7d and 8d).

Notably, the time courses of ΔR_1 and ΔR_2 were consistent among individual animals across different brain regions (Figures S4 and S5). The mean time courses were calculated without any signal normalization, ensuring that the characteristic relaxation (ΔR_1 and ΔR_2) responses were identified for each region.

4. Discussion

We present the first 3D MRF method to dynamically track the transport of Gd-DTPA in the mouse brain through simultaneous multi-parametric mapping. The MRF sequence presented in the current work was designed to accurately map T_1 and T_2 in both pre- and post-contrast mouse brains during DCE studies. The acquisition efficiency of the current sequence was significantly improved compared to that of previous preclinical MRF studies. We also exploited a subspace-based, low-rank reconstruction approach to improve the accuracy of parameter mapping. The accuracy of T_1 and T_2 mapping, validated by undersampled phantom data, was in agreement with the gold-standard methods. The highly reproducible results enabled fast, accurate, and simultaneous in vivo T_1 and T_2 measurements in small laboratory animals. With a 48-fold

undersampling, the MRF method allowed for dynamic tracking of the transport of intracisternally administered Gd-DTPA throughout the whole mouse brain, at a temporal resolution of 4 min 20 s and a spatial resolution of $192 \times 192 \times 500 \mu\text{m}^3$.

To date, only a limited number of studies focused on mapping T_1 in human or animal brains at 9.4 T,^{39–44} and even fewer studies measured T_2 at this field strength.^{12,17,43} In cases where both T_1 and T_2 were of interest, sequential scans were performed to map T_1 and T_2 in the mouse brain using conventional methods, which led to a total acquisition time of over 1 hr for a single slice of the brain.⁴³ The current method enabled whole-brain T_1 and T_2 mapping in mouse brain with a spatial resolution of $192 \times 192 \times 250 \mu\text{m}^3$ in 30 min. T_1 and T_2 measured by 3D MRF were in good agreement with the previous studies using both MRF and non-MRF mapping methods. The MRF-measured T_1 ranged from 1300 to 1500 ms in white matter and 1800 to 2000 ms in gray matter, while the T_2 ranged from 20 to 30 ms in white matter and 30 to 40 ms in gray matter. Further, the T_1 (3091 ± 168 ms) and T_2 (143.8 ± 17.2 ms) of ventricular CSF quantified by the current MRF sequence were similar to those reported in a previous study of macaque brain at the same field strength using a different MRF sequence and image reconstruction method.^{17,45}

The proposed MRF acquisition enabled dynamic and quantitative tracking of Gd-DTPA transport within the CSF pathway across the entire mouse brain. The observed time courses of ΔR_1 and ΔR_2 follow a linear relationship with the changes in Gd-DTPA concentration, enabling direct quantification of Gd-DTPA. This direct quantitative approach eliminates the need for signal normalization and reduces the impact of experimental variables such as animal positioning and coil loading. As a result, it leads to reduced signal variability when compared with previous studies employing semi-quantitative T_1 -weighted methods.³³ Previous studies have employed conventional T_1 mapping methods to track intravenously or intrathecally administered GBCAs in mouse brain, where least-square curve fitting of image intensities was performed to derive dynamic T_1 values.^{40,41,46} MRF offers a unique advantage that pattern matching between the acquired signal and the dictionary of simulated signals minimizes the effects of acquisition and undersampling errors while estimating multiple tissue parameters simultaneously.⁹ Although we only demonstrated 3D DCE-MRF's application in tracking a single contrast agent in the current study, the multiparametric nature of the MRF method has the potential to be extended to simultaneously track two contrast agents.^{16,47}

The 3D MRF method presented in the current study has significantly advanced whole-brain multiparametric mapping in mice. With a mouse brain about 2400 times smaller than the

human brain,⁴⁸ preclinical MRF development has been challenged by the drastically lower SNR compared to human studies. This limitation was overcome by a synergistic approach of improved MRF sequence design and advanced reconstruction method employing low-rank subspace modeling. Furthermore, iterative reconstruction on GPU power has substantially accelerated the image reconstruction process and facilitated the post-processing of DCE- MRF data, where a total of 32 time points (24,576 images) were acquired. Nevertheless, the spatial-temporal resolution of the current MRF method can be further improved by further optimization of the sequence to shorten the acquisition time for each fingerprint,^{49,50} as well as by implementation of more advanced reconstruction method,⁴⁵ and optimization of the sampling trajectory to enhance efficiency.^{51,52} These improvements hold the promise to further improve the spatial resolution for dynamic mapping while maintaining the same temporal resolution.

In conclusion, we present the first 3D MRF method for highly efficient and accurate T_1 and T_2 mapping of the entire mouse brain. This technique enables direct and quantitative tracking of contrast agent transport across various brain regions. Both acquisition and reconstruction efficiencies have been significantly improved compared to previous preclinical MRF studies. The proposed 3D MRF method holds the potential to greatly expand the capabilities of quantitative MRI in small animal imaging, with applications ranging from studies of CSF circulation to pharmacokinetics.

Acknowledgments

This work made use of the High Performance Computing Resource in the Core Facility for Advanced Research Computing at Case Western Reserve University. This work was supported by grants from the National Institute of Health awards R01 NS124206 to X. Y., and predoctoral fellowship award from American Heart Association 23PRE1017924 to Y. Z. W.Z. was supported in part by NIH training grants T32 EB007509, T32 GM007250, and TL1 TR000441.

Data availability statement

The experimental data, images, and code from this study are available upon request to the corresponding author.

References

1. Hoyer C, Gass N, Weber-Fahr W, Sartorius A. Advantages and Challenges of Small Animal Magnetic Resonance Imaging as a Translational Tool. *Neuropsychobiology*. 2014;69(4):187-

201. doi:10.1159/000360859
2. Watanabe T, Frahm J, Michaelis T. *In Vivo* Brain MR Imaging at Subnanoliter Resolution: Contrast and Histology. *Magn Reson Med Sci*. 2016;15(1):11-25. doi:10.2463/mrms.2015-0048
 3. Hattingen E, Jurcoane A, Nelles M, et al. Quantitative MR Imaging of Brain Tissue and Brain Pathologies. *Clin Neuroradiol*. 2015;25(S2):219-224. doi:10.1007/s00062-015-0433-8
 4. Brown RW, Cheng YN, Haacke EM, Thompson MR, Venkatesan R. *Magnetic Resonance Imaging: Physical Principles and Sequence Design*. 1st ed. Wiley; 2014. doi:10.1002/9781118633953
 5. Wood ML, Hardy PA. Proton relaxation enhancement. *J Magn Reson Imaging JMRI*. 1993;3(1):149-156. doi:10.1002/jmri.1880030127
 6. Wang HZ, Riederer SJ, Lee JN. Optimizing the precision in T1 relaxation estimation using limited flip angles. *Magn Reson Med*. 1987;5(5):399-416. doi:10.1002/mrm.1910050502
 7. Deoni SCL, Peters TM, Rutt BK. High-resolution T_1 and T_2 mapping of the brain in a clinically acceptable time with DESPOT1 and DESPOT2. *Magn Reson Med*. 2005;53(1):237-241. doi:10.1002/mrm.20314
 8. Peters AM, Brookes MJ, Hoogenraad FG, et al. T2* measurements in human brain at 1.5, 3 and 7 T. *Magn Reson Imaging*. 2007;25(6):748-753. doi:10.1016/j.mri.2007.02.014
 9. Ma D, Gulani V, Seiberlich N, et al. Magnetic resonance fingerprinting. *Nature*. 2013;495(7440):187-192. doi:10.1038/nature11971
 10. Poorman ME, Martin MN, Ma D, et al. Magnetic resonance fingerprinting Part 1: Potential uses, current challenges, and recommendations. *J Magn Reson Imaging*. 2020;51(3):675-692. doi:10.1002/jmri.26836
 11. Gao Y, Chen Y, Ma D, et al. Preclinical MR fingerprinting (MRF) at 7 T: effective quantitative imaging for rodent disease models: HIGH-FIELD PRECLINICAL MRF. *NMR Biomed*. 2015;28(3):384-394. doi:10.1002/nbm.3262
 12. Gu Y, Wang CY, Anderson CE, et al. Fast magnetic resonance fingerprinting for dynamic contrast-enhanced studies in mice. *Magn Reson Med*. 2018;80(6):2681-2690. doi:10.1002/mrm.27345
 13. Anderson CE, Wang CY, Gu Y, et al. Regularly incremented phase encoding – MR fingerprinting (RIPE-MRF) for enhanced motion artifact suppression in preclinical cartesian MR fingerprinting. *Magn Reson Med*. 2018;79(4):2176-2182. doi:10.1002/mrm.26865
 14. Buonincontri G, Sawiak SJ. MR fingerprinting with simultaneous B1 estimation. *Magn Reson Med*. 2016;76(4):1127-1135. doi:10.1002/mrm.26009

15. Driehuys B, Nouis J, Badea A, et al. Small Animal Imaging with Magnetic Resonance Microscopy. Published online 2009.
16. Anderson CE, Johansen M, Erokwu BO, et al. Dynamic, Simultaneous Concentration Mapping of Multiple MRI Contrast Agents with Dual Contrast - Magnetic Resonance Fingerprinting. *Sci Rep*. 2019;9(1):19888. doi:10.1038/s41598-019-56531-7
17. Gu Y, Wang L, Yang H, et al. Three-dimensional high-resolution T₁ and T₂ mapping of whole macaque brain at 9.4 T using magnetic resonance fingerprinting. *Magn Reson Med*. 2022;87(6):2901-2913. doi:10.1002/mrm.29181
18. Nezafat R, Stuber M, Ouwerkerk R, Gharib AM, Desai MY, Pettigrew RI. B1-insensitive T₂ preparation for improved coronary magnetic resonance angiography at 3 T. *Magn Reson Med*. 2006;55(4):858-864. doi:10.1002/mrm.20835
19. Jiang Y, Ma D, Seiberlich N, Gulani V, Griswold MA. MR fingerprinting using fast imaging with steady state precession (FISP) with spiral readout: MR Fingerprinting with FISP. *Magn Reson Med*. 2015;74(6):1621-1631. doi:10.1002/mrm.25559
20. MacAskill CJ, Markley M, Farr S, et al. Rapid B₁-Insensitive MR Fingerprinting for Quantitative Kidney Imaging. *Radiology*. 2021;300(2):380-387. doi:10.1148/radiol.2021202302
21. Ma D, Jiang Y, Chen Y, et al. Fast 3D magnetic resonance fingerprinting for a whole-brain coverage. *Magn Reson Med*. 2018;79(4):2190-2197. doi:10.1002/mrm.26886
22. Zhao B, Setsompop K, Adalsteinsson E, et al. Improved magnetic resonance fingerprinting reconstruction with low-rank and subspace modeling. *Magn Reson Med*. 2018;79(2):933-942. doi:10.1002/mrm.26701
23. Liang ZP. Spatiotemporal Imaging with Partially Separable Functions.
24. Uecker M, Lai P, Murphy MJ, et al. ESPIRiT—an eigenvalue approach to autocalibrating parallel MRI: Where SENSE meets GRAPPA. *Magn Reson Med*. 2014;71(3):990-1001. doi:10.1002/mrm.24751
25. Ong F, Lustig M. SigPy: A Python Package for High Performance Iterative Reconstruction. In: *Proceedings of International Society of Magnetic Resonance in Medicine 27th Annual Conference*. International Society of Magnetic Resonance in Medicine; 2019:4819.
26. Beck A, Teboulle M. A Fast Iterative Shrinkage-Thresholding Algorithm for Linear Inverse Problems. *SIAM J Imaging Sci*. 2009;2(1):183-202. doi:10.1137/080716542
27. Beck A, Teboulle M. Fast Gradient-Based Algorithms for Constrained Total Variation Image Denoising and Deblurring Problems. *IEEE Trans Image Process*. 2009;18(11):2419-2434. doi:10.1109/TIP.2009.2028250

28. Shewchuk JR. *An Introduction to the Conjugate Gradient Method Without the Agonizing Pain*. Carnegie Mellon University; 1994.
29. Fessler JA, Sutton BP. Nonuniform fast fourier transforms using min-max interpolation. *IEEE Trans Signal Process*. 2003;51(2):560-574. doi:10.1109/TSP.2002.807005
30. Wang G, Luo T, Nielsen JF, Noll DC, Fessler JA. B-Spline Parameterized Joint Optimization of Reconstruction and K-Space Trajectories (BJORK) for Accelerated 2D MRI. *IEEE Trans Med Imaging*. 2022;41(9):2318-2330. doi:10.1109/TMI.2022.3161875
31. Wang G, Shah N, Zhu K, Noll D, Fessler J. MIRTorch: A PyTorch-powered Differentiable Toolbox for Fast Image Reconstruction and Scan Protocol Optimization. In: *Proceedings of International Society of Magnetic Resonance in Medicine 31st Annual Conference*. International Society of Magnetic Resonance in Medicine; 2022:4982. doi:10.58530/2022/4982
32. Muckley MJ, Stern R, Murrell T, Knoll F. TorchKbNufft: A High-Level, Hardware-Agnostic Non-Uniform Fast Fourier Transform. In: *Proceedings of International Society of Magnetic Resonance in Medicine 5th Workshop on Data Sampling & Image Reconstruction*. International Society of Magnetic Resonance in Medicine; 2020.
33. Zhu Y, Wang G, Kolluru C, et al. Transport pathways and kinetics of cerebrospinal fluid tracers in mouse brain observed by dynamic contrast-enhanced MRI. *Sci Rep*. 2023;13(1):13882. doi:10.1038/s41598-023-40896-x
34. Ma Y, Hof PR, Grant SC, et al. A three-dimensional digital atlas database of the adult C57BL/6J mouse brain by magnetic resonance microscopy. *Neuroscience*. 2005;135(4):1203-1215. doi:10.1016/j.neuroscience.2005.07.014
35. Avants BB, Tustison NJ, Song G, Cook PA, Klein A, Gee JC. A reproducible evaluation of ANTs similarity metric performance in brain image registration. *NeuroImage*. 2011;54(3):2033-2044. doi:10.1016/j.neuroimage.2010.09.025
36. Hübner NS, Mechling AE, Lee HL, et al. The connectomics of brain demyelination: Functional and structural patterns in the cuprizone mouse model. *NeuroImage*. 2017;146:1-18. doi:10.1016/j.neuroimage.2016.11.008
37. Koch S, Mueller S, Foddiss M, et al. Atlas registration for edema-corrected MRI lesion volume in mouse stroke models. *J Cereb Blood Flow Metab*. 2019;39(2):313-323. doi:10.1177/0271678X17726635
38. Cao X, Liao C, Wang Z, et al. A model-based velocity mapping of blood flow using MR fingerprinting. In: *Proceedings of International Society of Magnetic Resonance in Medicine 25th Annual Conference*. International Society of Magnetic Resonance in Medicine;

- 2017:0941.
39. Lee H, Mortensen K, Sanggaard S, et al. Quantitative Gd-DOTA uptake from cerebrospinal fluid into rat brain using 3D VFA-SPGR at 9.4T: Quantitative Gd-DOTA Uptake from CSF into Rat Brain. *Magn Reson Med*. 2018;79(3):1568-1578. doi:10.1002/mrm.26779
 40. Xue Y, Liu X, Koundal S, et al. In vivo T1 mapping for quantifying glymphatic system transport and cervical lymph node drainage. *Sci Rep*. 2020;10(1):14592. doi:10.1038/s41598-020-71582-x
 41. Xue Y, Gursky Z, Monte B, et al. Sustained glymphatic transport and impaired drainage to the nasal cavity observed in multiciliated cell ciliopathies with hydrocephalus. *Fluids Barriers CNS*. 2022;19(1):20. doi:10.1186/s12987-022-00319-x
 42. Hagberg G, Bause J, Ethofer T, et al. Whole brain MP2RAGE-based mapping of the longitudinal relaxation time at 9.4T. *NeuroImage*. 2017;144:203-216. doi:10.1016/j.neuroimage.2016.09.047
 43. Kuo YT, Herlihy AH, So PW, Bhakoo KK, Bell JD. In vivo measurements of T1 relaxation times in mouse brain associated with different modes of systemic administration of manganese chloride. *J Magn Reson Imaging*. 2005;21(4):334-339. doi:10.1002/jmri.20285
 44. van de Ven RCG, Hogers B, van den Maagdenberg AMJM, et al. T1 relaxation in in vivo mouse brain at ultra-high field. *Magn Reson Med*. 2007;58(2):390-395. doi:10.1002/mrm.21313
 45. Gu Y, Pan Y, Fang Z, et al. Deep learning-assisted preclinical MR fingerprinting for sub-millimeter T₁ and T₂ mapping of entire macaque brain. *Magn Reson Med*. 2024;91(3):1149-1164. doi:10.1002/mrm.29905
 46. Herrmann K, Erokku BO, Johansen ML, et al. Dynamic Quantitative T1 Mapping in Orthotopic Brain Tumor Xenografts. 2016;9(2).
 47. Anderson CE, Donnola SB, Jiang Y, et al. Dual Contrast - Magnetic Resonance Fingerprinting (DC-MRF): A Platform for Simultaneous Quantification of Multiple MRI Contrast Agents. *Sci Rep*. 2017;7(1):8431. doi:10.1038/s41598-017-08762-9
 48. Herfert K, Mannheim JG, Kuebler L, et al. Quantitative Rodent Brain Receptor Imaging. *Mol Imaging Biol*. 2020;22(2):223-244. doi:10.1007/s11307-019-01368-9
 49. Heesterbeek DGJ, Koolstra K, van Osch MJP, van Gijzen MB, Vos FM, Nagtegaal MA. Mitigating undersampling errors in MR fingerprinting by sequence optimization. *Magn Reson Med*. 2023;89(5):2076-2087. doi:10.1002/mrm.29554
 50. Jordan SP, Hu S, Rozada I, et al. Automated design of pulse sequences for magnetic resonance fingerprinting using physics-inspired optimization. *Proc Natl Acad Sci*.

51. Wang G, Nielsen J, Fessler JA, Noll DC. Stochastic optimization of three-dimensional non-Cartesian sampling trajectory. *Magn Reson Med.* 2023;90(2):417-431. doi:10.1002/mrm.29645
52. Cao X, Liao C, Iyer SS, et al. Optimized multi-axis spiral projection MR fingerprinting with subspace reconstruction for rapid whole-brain high-isotropic-resolution quantitative imaging. *Magn Reson Med.* 2022;88(1):133-150. doi:10.1002/mrm.29194

Figures and captions

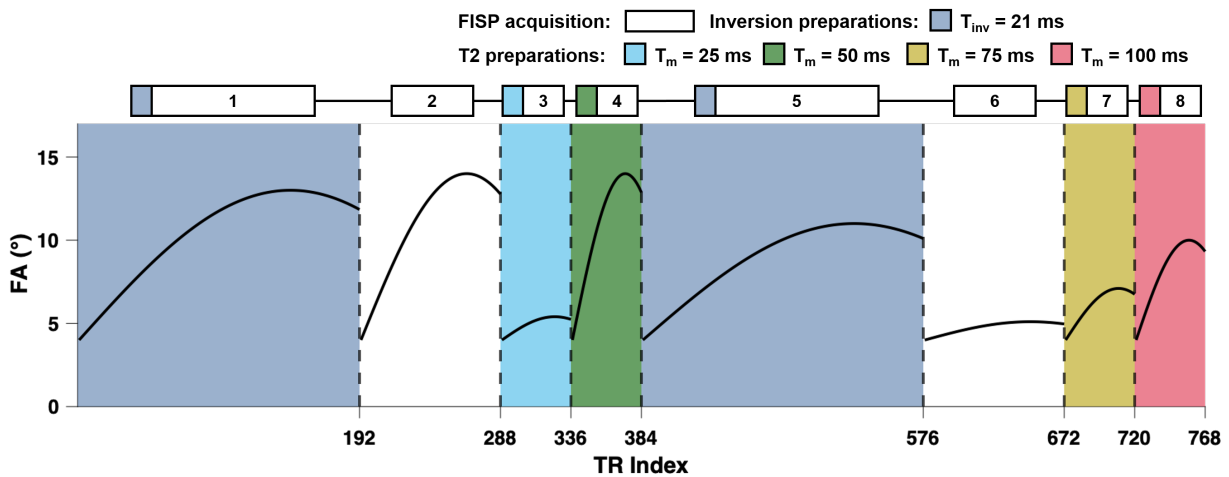


Figure 1. Schematics and flip angle pattern of the MR fingerprinting (MRF) sequence. Fast imaging with steady-state precession, FISP. Inversion delay, T_{inv} . Mixing time, T_m .

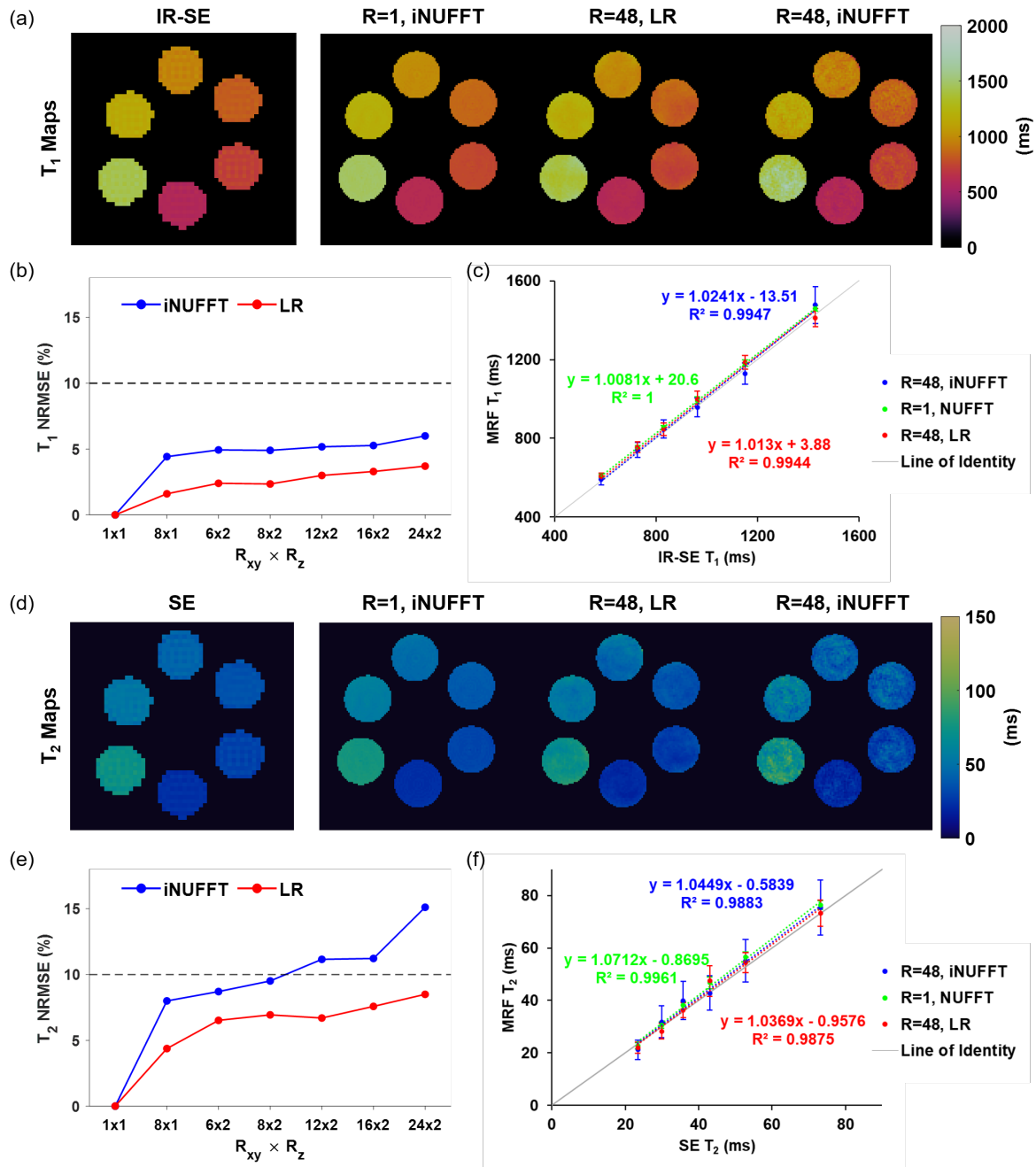


Figure 2. In vitro validation. (a) T₁ maps from inversion-recovery spin-echo (IR-SE) in comparison with fully sampled MRF reconstructed with inverse NUFFT (iNUFFT) and 48-fold undersampled MR fingerprinting (MRF) reconstructed with low-rank (LR) approach and iNUFFT, respectively. (b) Normalized root-mean-square error (NRMSE) of T₁ maps of a phantom with varied combinations of in-plane (R_{xy}) and through-plane (R_z) undersampling schemes. (c) Correlations between MRF-measured and IR-SE-measured T₁ values. (d) T₂ maps from spin-echo (SE) in comparison with MRF-derived maps. (e) NRMSE of T₂ maps of a phantom with varied undersampling schemes. (f) Correlations between MRF-measured and SE-measured T₂ values. The dashed lines in (b) and (e) indicate 10% NRMSE.

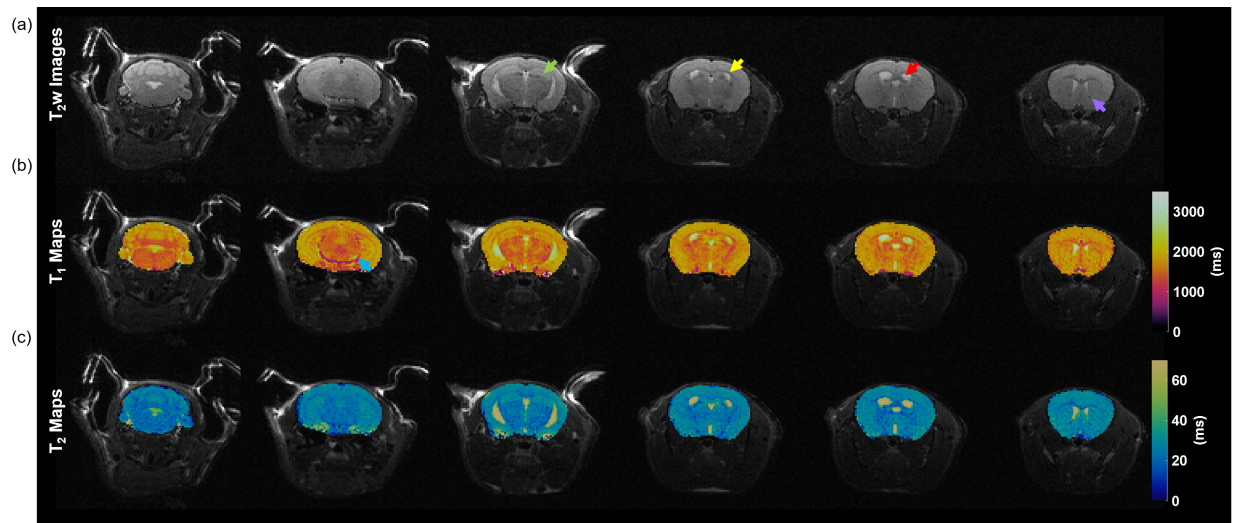


Figure 3. T₁ and T₂ maps of mouse brain by 3D MR fingerprinting (MRF) from axial view. **(a)** T₂-weighted images of a representative mouse brain as axial slices from posterior to anterior direction. **(b-c)** Corresponding T₁ and T₂ maps of the representative mouse brain. Arrows indicate landmark anatomical structures in the brain: Green, hippocampus; Yellow, corpus callosum; Red, ventricular system; Purple, anterior commissure; Blue, posterior cerebral artery.

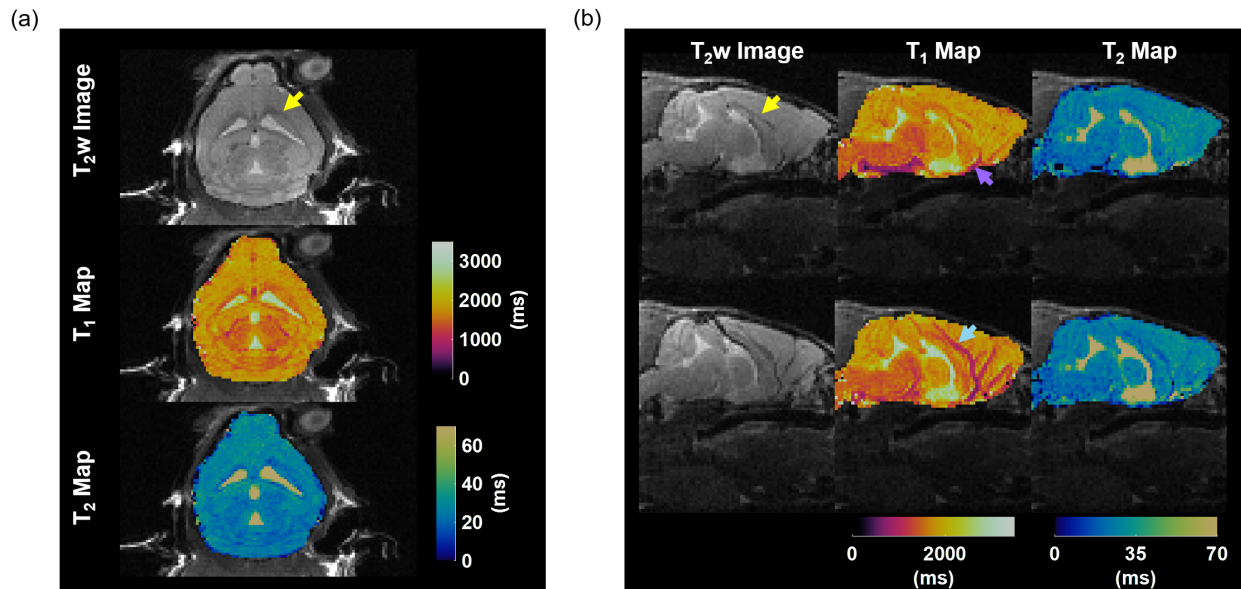


Figure 4. T₁ and T₂ maps of mouse brain by 3D MR fingerprinting (MRF) from coronal and sagittal views. **(a)** T₂-weighted (T_{2w}) image, T₁ map, and T₂ map of a center coronal slice. **(b)** T_{2w} images, T₁ maps, and T₂ maps of two center sagittal slices. Arrows indicate landmark anatomical structures in the brain: Yellow, corpus callosum; Purple, anterior cerebral artery; Blue, middle cerebral artery.

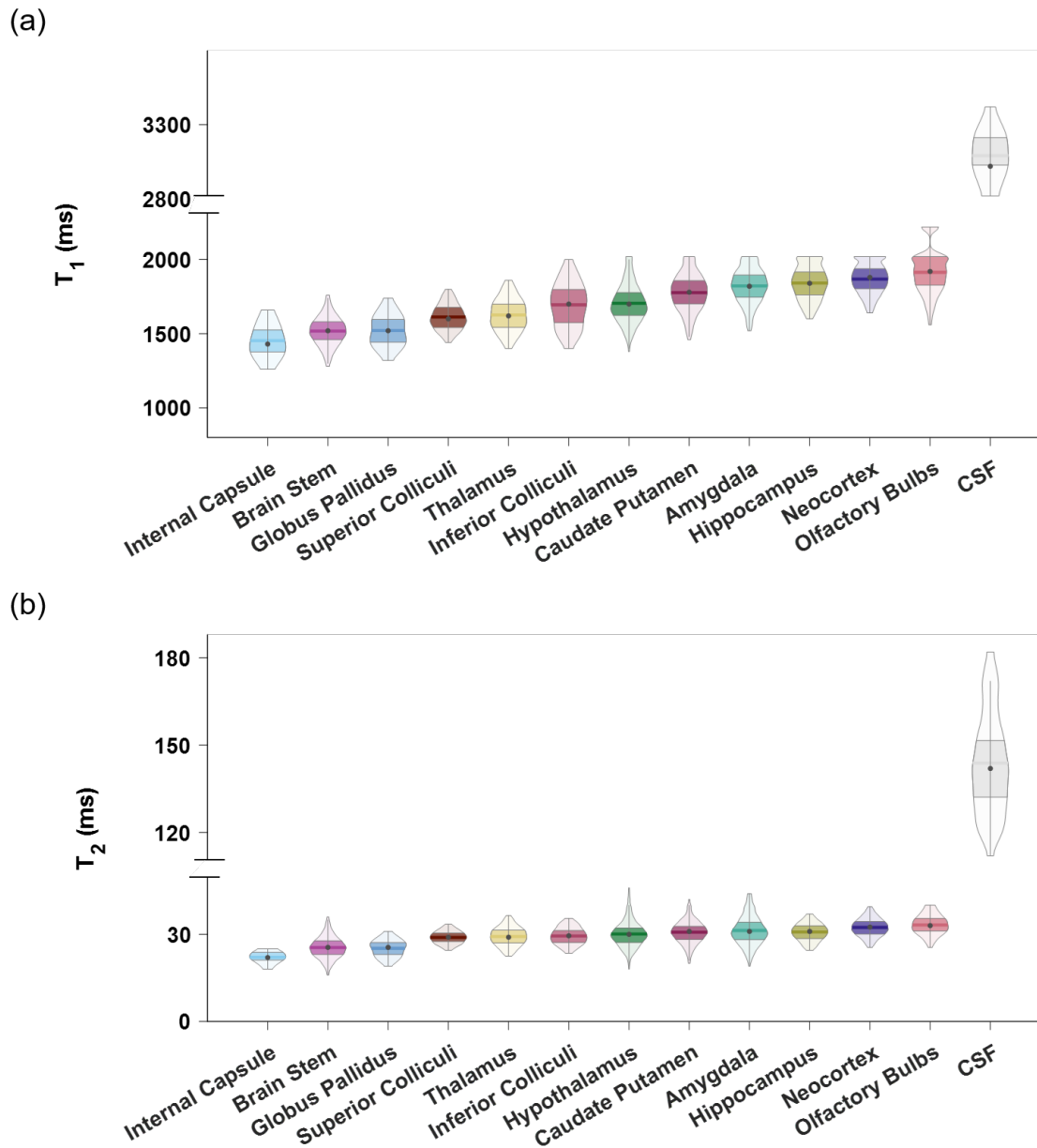


Figure 5. Mean T_1 (a) and T_2 (b) values in selected regions of interest across the mouse brain ($n = 3$). Solid dots represent median T_1 and T_2 values. Solid horizontal lines represent mean T_1 and T_2 values. CSF, cerebrospinal fluid.

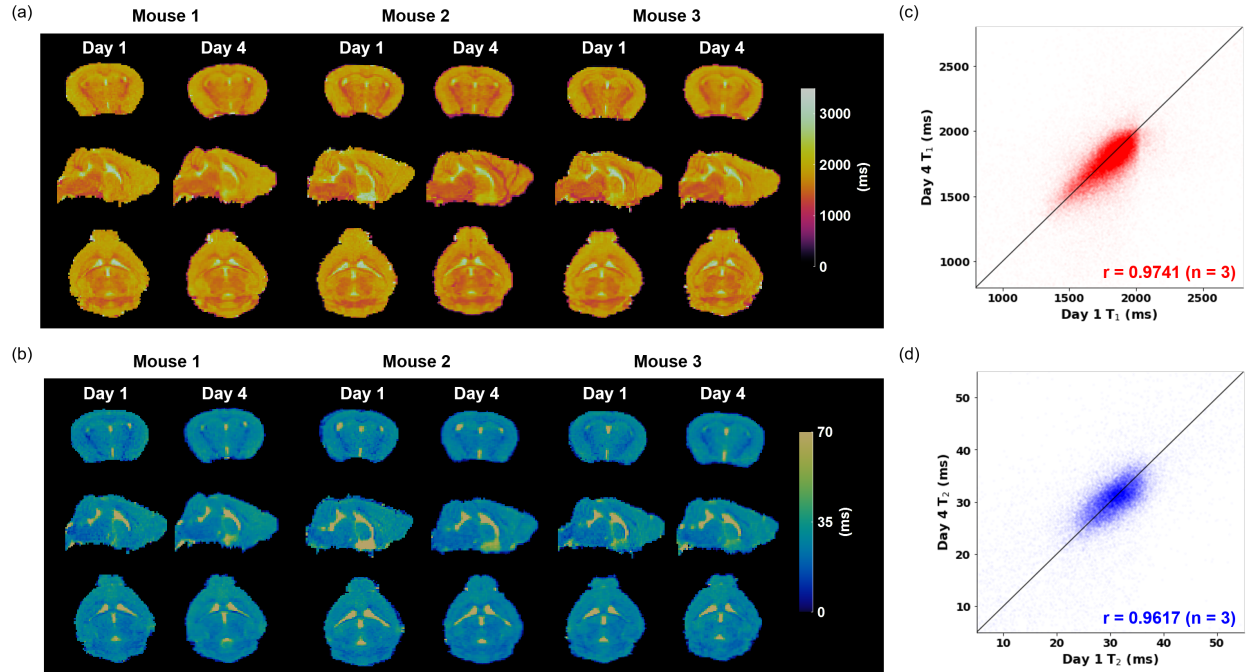


Figure 6. Repeatability of in vivo 3D MR fingerprinting (MRF) measurements. **(a-b)** T₁ **(a)** and T₂ **(b)** maps of three orthogonal slices acquired from two repeated MRF measurements in three animals. The scans were conducted three days apart. **(c-d)** Voxel-wise comparison of T₁ **(c)** and T₂ **(d)** measurements from two repeated scans of all animals. The black lines represent the lines of identity. r , correlation coefficient.

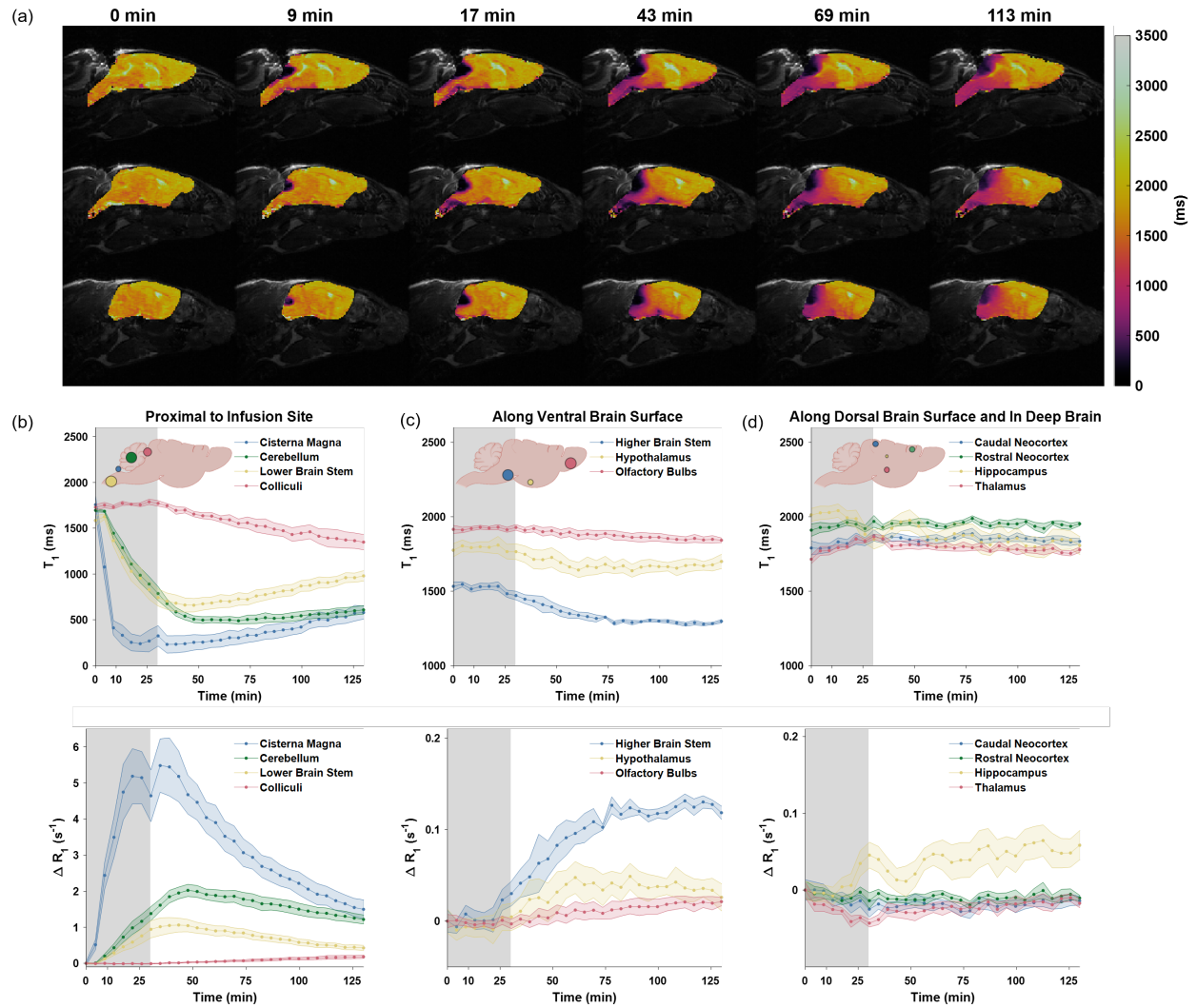


Figure 7. Brain-wide dynamic T₁ and ΔR₁ changes induced by Gd-DTPA. (a) Representative sagittal views of T₁ maps overlaid on T₂-weighted images from one animal at selected time points. (b-d) Time courses of T₁ and ΔR₁ changes in selected ROIs. Gray bands indicate the time period of Gd-DTPA infusion. Colored lines represent the mean T₁ and ΔR₁ changes (n=5). Shaded areas represent standard errors.

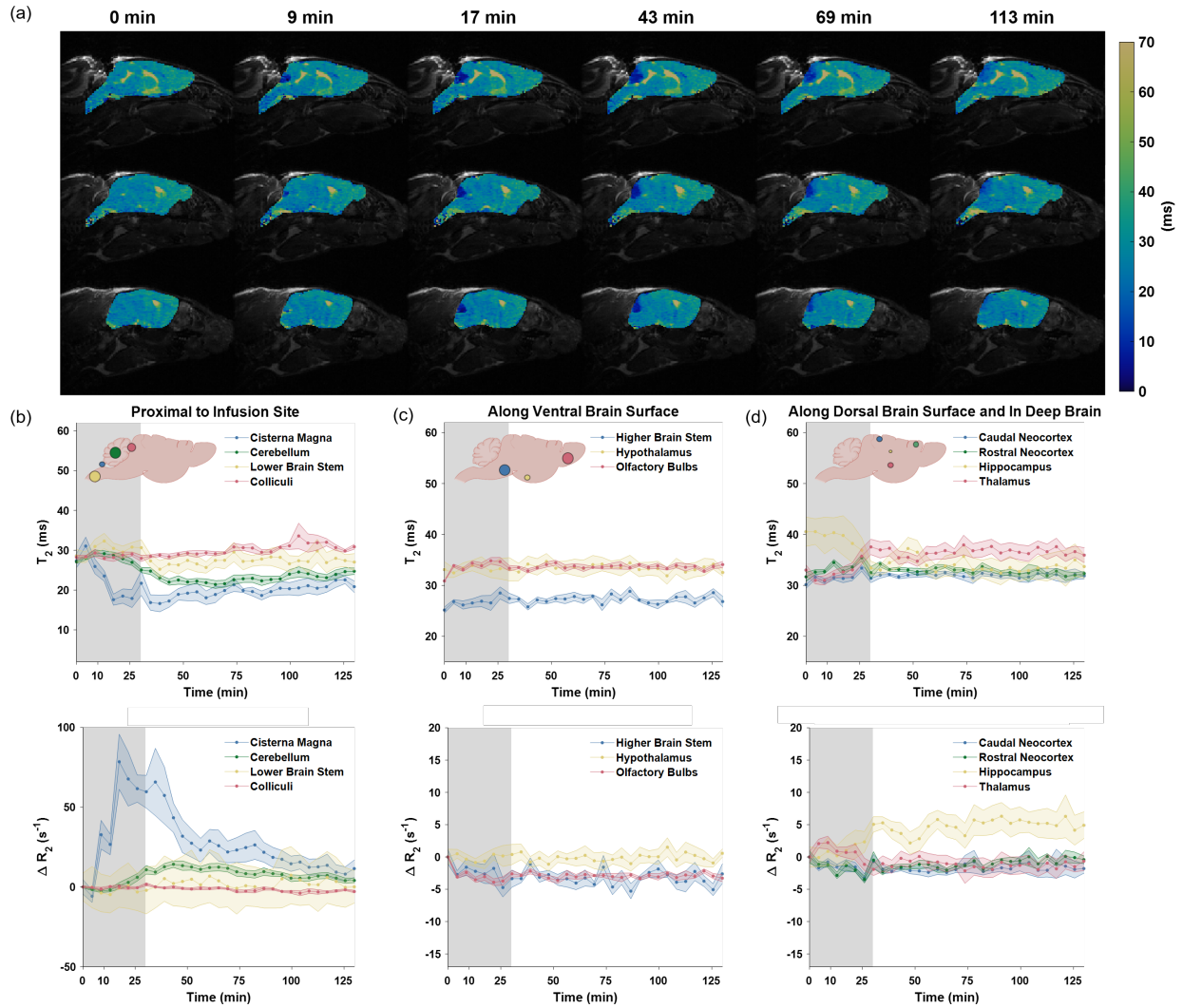


Figure 8. Brain-wide dynamic T_2 and ΔR_2 changes induced by Gd-DTPA. **(a)** Representative sagittal views of T_2 maps overlaid on T_2 -weighted images from one animal at selected time points. **(b-d)** Time courses of T_2 and ΔR_2 changes in selected ROIs. Gray bands indicate the time period of Gd-DTPA infusion. Colored lines represent the mean T_2 and ΔR_2 changes ($n=5$). Shaded areas represent standard errors.

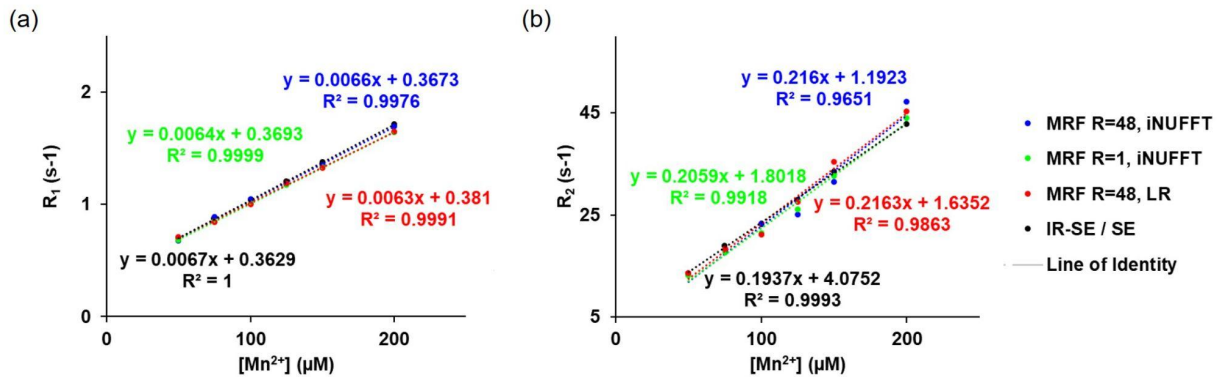


Figure S1. Correlation of relaxation rates and Mn^{2+} concentrations. (a) Correlation of Mn^{2+} concentration and R_1 derived from 3D MR fingerprinting (MRF) and inverse-recovery spin echo (IR-SE) methods. (b) Correlation of Mn^{2+} concentration and R_2 derived from MRF and spin-echo (SE) methods.

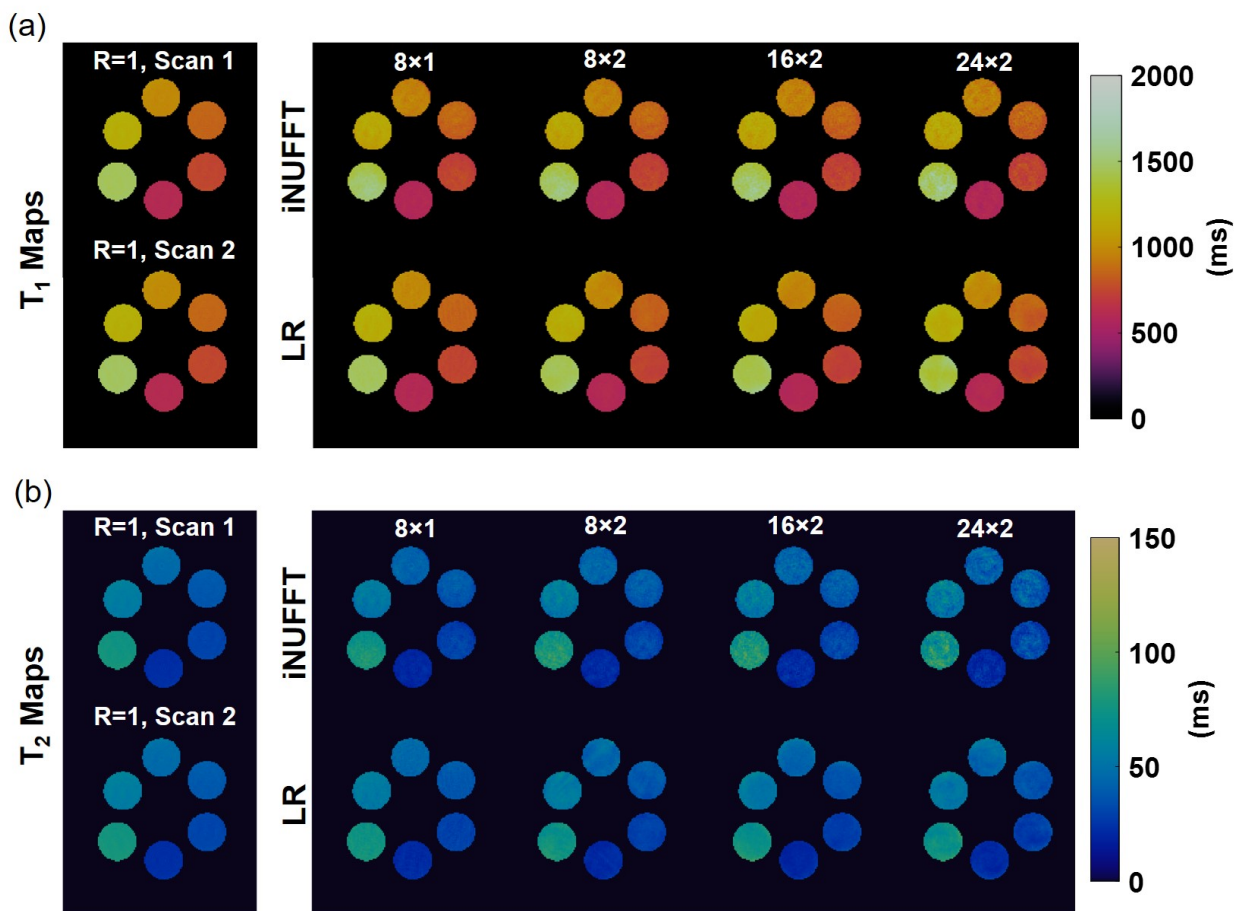


Figure S2. T_1 and T_2 results from fully sampled and undersampled MR fingerprinting (MRF) scans. (a) T_1 maps from two fully sampled MRF scans and those from undersampled scans with varied in-plane (R_{xy}) and through-plane (R_z) undersampling factors, reconstructed with inverse non-uniform Fourier transform (iNUFFT) and low-rank (LR) subspace modeling. (b) T_2 maps from two fully sampled MRF scans and those from undersampled scans with varied R_{xy} and R_z undersampling factors, reconstructed with iNUFFT and LR.

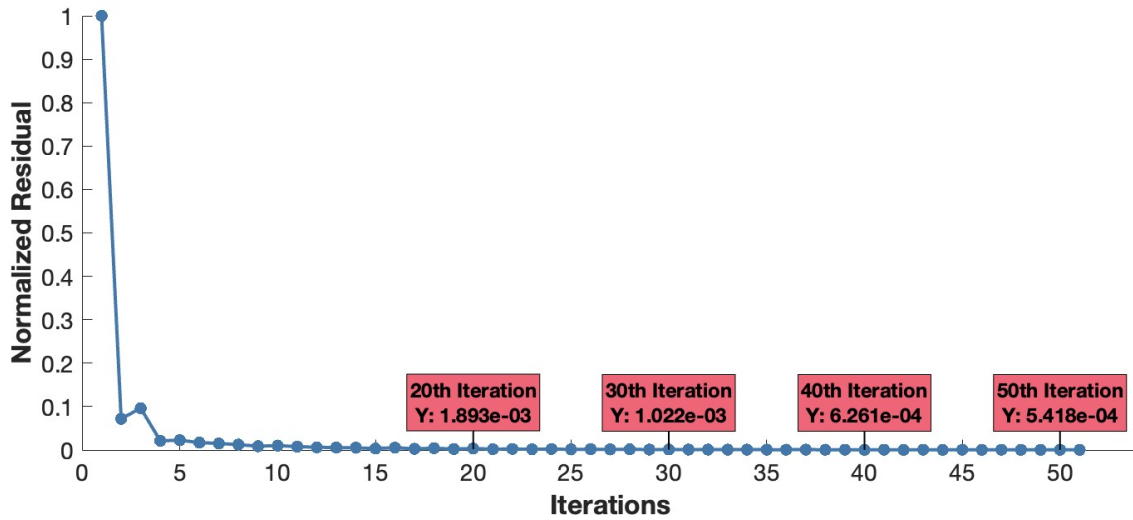


Figure S3. Normalized residuals over conjugate gradient (CG) iterations for subspace-based image reconstruction via low rank (LR) for MR fingerprinting (MRF) acquired at 48-fold undersampling. Normalized residual is defined as $\|AU\hat{V} - y\| / \|y\|$.

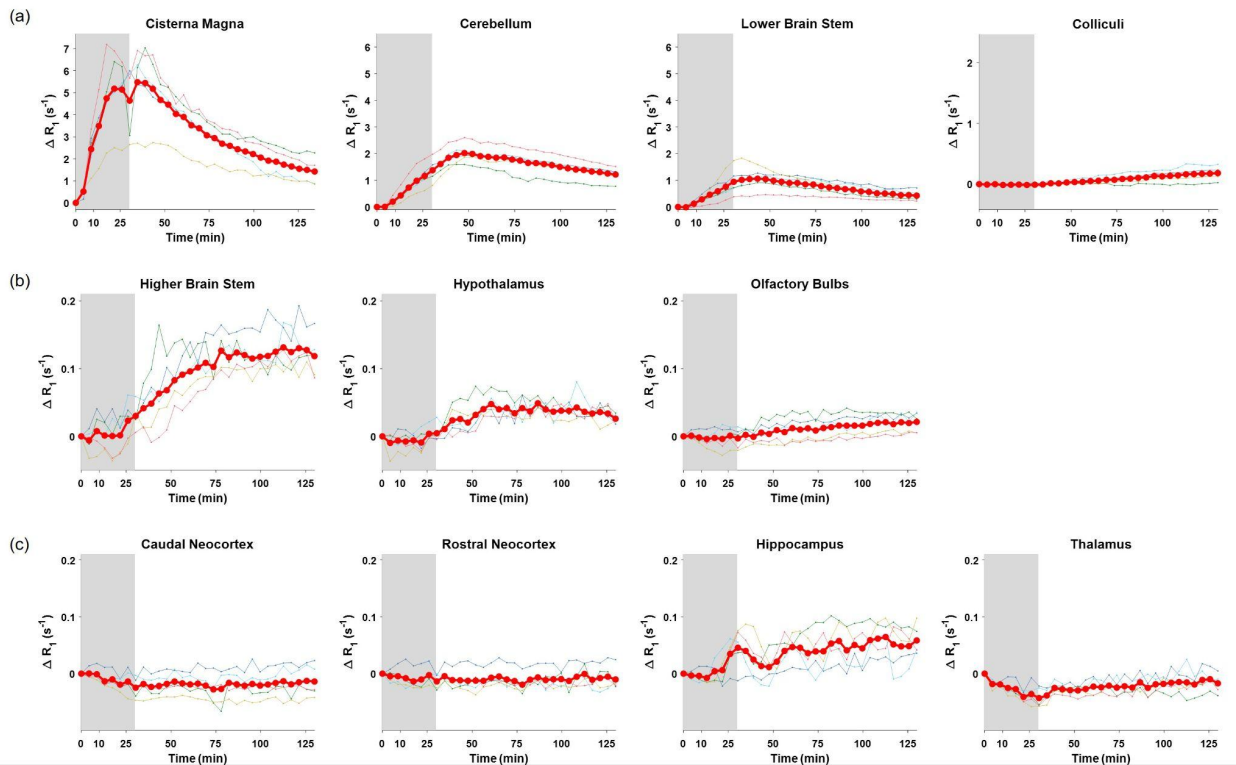


Figure S4. Time courses of ΔR_1 changes in selected ROIs following Gd-DTPA infusion at cisterna magna. (a) Proximal to the infusion site. (b) Along the ventral brain surface. (c) Along the dorsal brain surface and in the deep brain. The individual animal data ($n = 5$) are plotted as thin lines, and the mean data are plotted as thick red lines. Shaded areas represent standard errors.

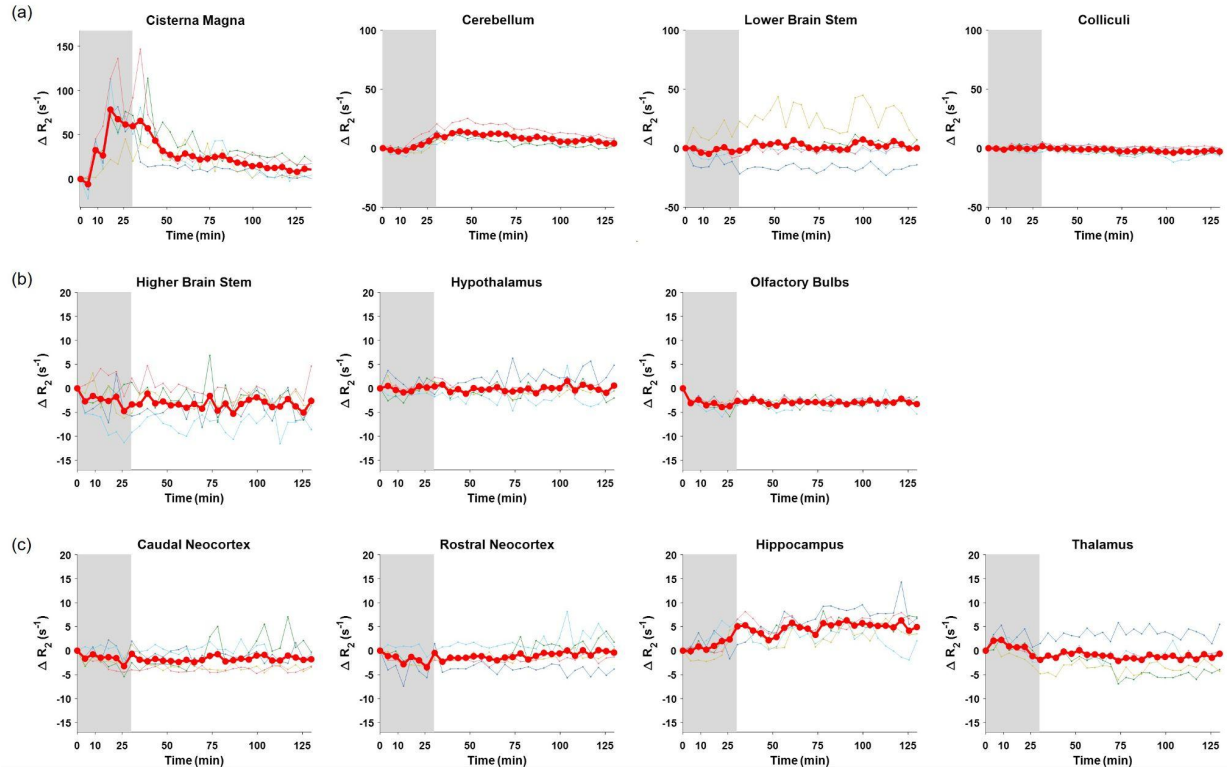


Figure S5. Time courses of ΔR_2 changes in selected spherical volumes placed at different brain regions following Gd-DTPA infusion at cisterna magna. (a) Proximal to the infusion site. (b) Along the ventral brain surface. (c) Along the dorsal brain surface and in the deep brain. The individual animal data ($n = 5$) are plotted as thin lines, and the mean data are plotted as thick red lines. Shaded areas represent standard errors.